Available online at www.sciencedirect.com

ScienceDirect

ELSEVIER

International Journal of Multiphase Flow 32 (2006) 1160–1181

International Journal of Multiphase Flow

www.elsevier.com/locate/ijmulflow

Comprehensive experimental investigation of the hydrodynamics of large-scale, 3D, oscillating bubble plumes

M. Simiano [a,b], R. Zboray [a], F. de Cachard [a], D. Lakehal [b,1],
G. Yadigaroglu [b,*]

[a] *Thermal-Hydraulics Laboratory, Paul Scherrer Institut, CH-5232 Villigen PSI, Switzerland*
[b] *Nuclear Engineering Laboratory, Institute of Energy Technology, Swiss Federal Institute of Technology,*
ETH, ETH-Zentrum, CLT, CH-8092 Zurich, Switzerland

Received 1 February 2005; received in revised form 24 May 2006

Abstract

An extensive study of the most important hydrodynamic characteristics of fairly large-scale bubble plumes was conducted using several measurement techniques and a variety of tools to analyze the data. Particle image velocimetry (PIV), double-tip optical probes (OP) and photographic techniques were extensively applied to measure bubble and liquid velocities, void-fraction and bubble sizes. PIV measurements in a vertical plane crossing the centre of the injector provided the instantaneous velocity fields for both phases, as well as hydrodynamic parameters, such as the movement of the axis of the plume and its instantaneous shape. Statistical studies were performed using image processing to determine the distribution of the apparent instantaneous plume diameter and centreline position. An important finding was that there is little instantaneous spreading of the bubble plume core; the spreading of the time-averaged plume width (as measured from the time-averaged void-fraction and time-averaged liquid velocity fields) is largely due to plume meandering and oscillations. The liquid-phase stress tensor distributions obtained from the instantaneous velocity data indicate that, for the continuous phase, these stresses scale linearly with the local void-fraction in the range of $0.5\% < \alpha < 2.5\%$. The bubbles were found to be ellipsoidal, with shape factor $e \approx 0.5$.

Keywords: Bubble plume; PIV; Reynolds stress tensor; Bubble dynamics; Bubbly flow; Meandering; Plume oscillation

1. Introduction

Bubbly flows can be found in many industrial processes, nuclear power and chemical plants, stirred reactors and bioreactors. Concrete examples in nuclear power plants can be found in the pressure suppression pools of

---

[*] Corresponding author. Present address: ETH, WEN, Weinbergstr. 94, CH-8006 Zurich, Switzerland. Tel.: +41 1 6324615; fax: +41 1 6321105.

E-mail address: yadi@ethz.ch (G. Yadigaroglu).

[1] Present address: ASCOMP GmbH, Technoparkstr. 1, CLT, CH-8005 Zurich, Switzerland.

0301-9322/$ - see front matter © 2006 Elsevier Ltd. All rights reserved.
doi:10.1016/j.ijmultiphaseflow.2006.05.014

Boiling Water Reactors. In passive BWRs, under accident conditions, venting of steam and/or non-condensable gases into the suppression pool may take place (Arnold et al., 1997). Walsche and Cachard (2000) investigated these venting phenomena.

In chemical bubble column reactors, bubbly flows are used to mix the flow and increase the efficiency of the reactions. Bubble column reactors are often used because of their simple construction, low operating cost and excellent heat transfer characteristics at immersed surfaces (Shah et al., 1982). Gas injection into liquid reservoirs has been also widely used to promote mixing, for example in current steel-making and lake de-stratification processes (Castillejos and Brimacombe, 1987; Sheng and Irons, 1992; Mory and Sano, 1981; Iguchi et al., 1992; Goossens, 1979). In all these applications, the main interest was to predict the currents induced by the dispersed phase evolving in the liquid and to determine the resulting mixing. Clearly, the performance of all these systems is considerably influenced by the motions of the bubbles and their interactions with the liquid flow, it is therefore important to understand these effects at the microscopic, local level also.

Various detailed experimental investigations have already been performed in bubbly flows, especially confined bubbly flows in pipes, in 2D plumes and in bubble columns (Hassan et al., 1992; Rensen and Roig, 2001; Delnoj et al., 1999). In these cases, on top of the coupled bubble–liquid interaction mechanism, effects like wall-induced turbulence and the direct influence of the wall on the bubble trajectories are also pertinent.

Comparatively fewer studies were focused on non-confined or weakly confined bubbly flows (Milgram, 1983; Kobus, 1968) where the absence of the wall leaves the plume free, and its boundaries oscillate in three dimensions, changing also the two-phase flow behaviour and producing instabilities and bubble cluster structures drifting the bubbles. Moreover, the production and the dissipation of large-scale bubble clusters and motions resulting from buoyancy forces depend on the initial conditions at the level of the bubble injecting device, so that a very careful control of the steadiness and uniformity of initial (injector) conditions is needed in performing such experiments.

In real technical applications, often the scales of bubble plumes and the containing vessels are such as to bring them in between the confined and non-confined flows. In these cases, bubbly flows often exhibit strong three-dimensional (3D) fluctuations and are influenced by the superposition of different characteristic length scales. As the effects of scale and of the instability on the 3D flow structure are complex, there is a need to conduct studies in large facilities closer in scale to real industrial applications. Clearly non-confined and weakly confined 3D bubble plumes are more complex and challenging to study. In particular, the 3D unstable, time-dependent behaviour of such flows is less understood than their global time-average characteristics and it offers interesting possibilities for the study of the basic local behaviour of unsteady two-phase flows, that were not addressed in previous bubble plume studies.

Most of the previous mentioned studies were focused on bubbly flows in a void-fraction range below 0.2%. The experiments reported here cover a void-fraction range of about 0.5–4%.

Recently, several new techniques and upgraded algorithms of PIV (particle image velocimetry) or PTT (particle tracking technique) were used to study the flow structures in bubbly flow, but almost all these studies were performed at small scales or on 2D systems where global instabilities played a minor role (Hassan and Canaan, 1991; Keane and Adrian, 1990).

This paper addresses in detail and in a comprehensive way both the local and global hydrodynamic behaviour of bubble plumes in a large vessel, and presents accurate estimations of the most important hydrodynamic parameters under well defined and controlled injection conditions. Statistical studies were also performed using image processing to determine the statistical distributions of the instantaneous plume diameter and of the position of its axis. Details about the project and additional issues addressed can be found in Simiano (2005).

2. Experimental setup

The bubble plume is produced in a metallic vessel called LINX, filled with demineralized water, Fig. 1. The vessel is 2 m in diameter and 3.4 m in height with a total volume of 9.4 m^3; 12 glass windows allow visual observations from outside, as well as the use of non-intrusive techniques such as photography, PIV, etc.

The bubble plume was produced by a sophisticated injection device, consisting of 716 needles with an outside diameter of 2 mm, uniformly distributed over a circular horizontal plate of 0.3 m in diameter. The needles

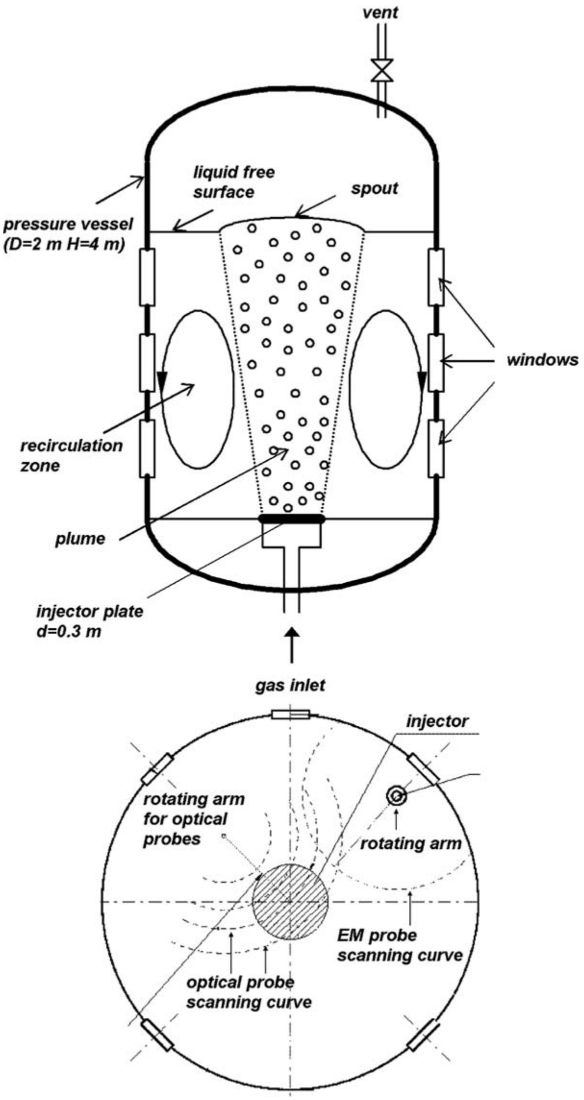

Fig. 1. Bubble plume experiment in the LINX facility.

were fed from the laboratory air supply through 0.8-m-long, 0.2-mm-diameter capillary tubes that throttle the gas flow and produce uniform gas distribution and bubble generation; a bubble plume with uniform properties over its cross-section and a narrow bubble size distribution, in a range of few millimeters, was obtained. The bubble size distributions are examined in detail later.

The size of the plume is relatively small compared to the size of the vessel, so that the plume can be considered as weakly confined.

The coordinate system used is defined by the following notation: the vertical coordinate is denoted as elevation or Y and it is always measured from the top of the injector; the horizontal coordinate is denoted as X when no radial symmetry is assumed and r otherwise. The vertical and horizontal velocity components are denoted as v and u, respectively.

3. Test matrix

A test matrix was set up to systematically examine the influence of the key parameters, gas injection rate and pool height, on the behaviour of the bubble plume. Table 1 gives also the time-averaged void-fraction

Table 1
Test matrix

Air mass flow rate (Nliter/min)	7.5	15	30	60
Air mass flux over injector area (g/m^2 s)	2.285	4.57	9.15	18.3
Immersion depths (m)	1.5, 2.0	1.5, 2.0	1.5, 2.0	1.5, 2.0
α_0 at $Y = 151$ mm (%)	0.582	1.05	1.975	4.06
α_s at $Y = 151$ mm (%)	0.350	0.719	1.309	2.480

at the injector centreline, α_0, and the time-averaged and cross-sectional void-fraction, α_s, obtained from measurements over a chord length $X = -200$ to 200 mm.

All data presented in this paper were collected with the immersion depth of 1.5 m. There were no significant differences with the 2.0 m immersion depth.

4. PIV technique

The PIV system used in our experiments for the velocity field estimations (Adrian, 1991) is commercial TSI equipment with a dual Yag laser (532 nm, 100 mJ) and a 1 × 1 kpixel camera with one-byte gray level (Kodak ES 1.0). This system is able to record and process in two-frame cross-correlation mode up to 15 pairs of pictures per second. PIV was originally designed for single-phase flow applications, but it has produced in the last decade promising results for multiphase flows too (Hassan et al., 1992; Delnoj et al., 1999; Hassan and Canaan, 1991). Glass filters fixed on the camera lens were used to select either the laser light reflected by the bubbles or the light emitted by fluorescent seeding particles sprinkled in the liquid and excited by the laser. This allowed (non-simultaneous) measurements of the velocity fields of both phases. The laser produced a 2-mm-thick vertical light sheet placed at the centre of the bubble injector. As seeding, 40 μm polymethyl methacrylate (PMMA) fluorescent particles (Rhodamine B as fluorescent substance) were used, with a density of 1.19 g/cm^3 and a refractive index of 1.48. These particles emit orange light (maximum of emission at 584 nm) when excited by green light (maximum of excitation at 560 nm). The size of seeding particles was chosen as a compromise between visibility, which is also related to the emitted light intensity, and their capability to follow the flow.

Examples of bubble and liquid PIV pictures are shown in Fig. 2. These pictures were preprocessed by removing the background and increasing the contrast with a linear transformation. This procedure strongly improved the cross-correlation results and removed also the black holes in the liquid pictures due to the presence of bubbles.

The plume was studied at three different elevations using three corresponding windows (Fig. 1). For each window view and for each experimental run (Table 1), 4000 pairs of images were taken at a frequency of

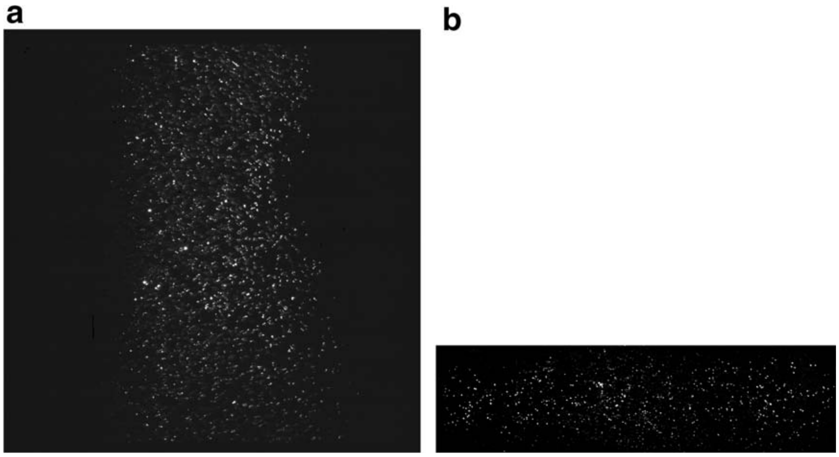

Fig. 2. Processed PIV images, recorded above the injector device at the 60 Nliter/min flow rate. The size of the image is 400 × 400 mm (bubble fields) and 40 × 290 mm (liquid field). (a) Bubbles and (b) seeding particles in the liquid phase.

0.5 Hz (about 133-min measurements), and 500 pairs at 15 Hz (33 s observation time). For the bubble velocity measurements, the field was about 400 × 400 mm with a resolution of 408 μm/pixel; each velocity vector was calculated over an interrogation region (IR) of 32 × 32 pixels (around 13 × 13 mm) with 50% overlapping. The total vector field consisted of 61 columns by 62 rows of vectors placed at the centre of their interrogation areas.

For the liquid velocity measurements, the vertical spread of the laser beam was significantly reduced to obtain higher light intensity, which explains the smaller PIV picture (Fig. 2b), so that the liquid flow field was about 40 × 290 mm with a resolution of 291 μm/pixel; each vector was calculated over an IR of 16 × 16 pixels (around 4.6 × 4.6 mm) with no overlapping (not needed for the smaller, liquid IR's).

The measurement occurrence rate in the first half of the plume (the region close to the laser) was quite constant (98%), as the number of emitting particles was sufficient for an accurate correlation. In the other half of the bubble plume, where the laser light intensity was lower, the occurrence rate was around 40%. The lack of excited particles was due to light attenuation caused by instantaneous increases of the local void-fraction, due for instance, to the presence of a bubble swarm. In the low-occurrence-rate zone, velocity measurements were not considered reliable as a selective underestimation of the liquid velocity took place. Indeed, the measurement failures corresponded to high instantaneous void fractions, which induce high bubble and surrounding-liquid velocities. Thus, higher velocities had a lesser probability to be detected. For that reason, only half of the liquid velocity profile was considered as sufficiently accurate. The other half (the region far from the laser) was plotted by mirroring, assuming radial symmetry for the time-averaged velocities. This assumption is also supported by the symmetry of the measured average PIV bubble velocity profiles, which will be discussed below.

5. Photographic technique

A photographic campaign was carried out through the vessel windows, using a macro lens, for visualization and quantitative investigation of bubble characteristics. The pictures were taken with back lightening produced by three 7.5 × 7.5 cm LED screens placed inside the vessel on a supporting rotating arm, Fig. 1. The camera used was a D-100 Nikon with a 200-mm-focal-length lens. The depth of field was estimated to be about 2–3 cm via a calibration target placed just in front of the illuminating screens. Typical exposures are shown in Fig. 3, where resolution was about 40 μm/px.

The bubble characteristic lengths were estimated by using two different methods. In both methods, a pattern recognition technique, implemented in a Matlab routine, was used to detect and analyze each single bubble and estimate its perimeter and projected area. In the first method, the perimeter was fitted with an ellipse using an analytical formulation; the principal axes and the inclination of the axis of the ellipse were estimated. As a large number of bubble images were processed, the probability density function (pdf) of the size of the principal axis sizes of the bubbles could be obtained, Fig. 4. Otherwise avoiding the assumption of ellipsoidal shape, 2D bubble objects (projection of the actual bubbles) were detected by using image enhancement and shape detection techniques, again implemented in a Matlab routine. With this second method, the inertia tensor and its two eigenvalues were determined with respect to the centre of mass of the bubble object. Thus the bubble size was determined along the two principal axes of inertia without requiring any assumptions on bubble shape. In the case of a strongly deformed ("wobbling") bubble, the difference between the two methods may be considerable, otherwise for the less deformed bubbles, the differences were much smaller. In Fig. 4, the distributions of the two axes of the bubbles are reported for both methods. Indeed, the estimations compare quite well, showing that the assumption of ellipsoidal shape was reasonable (this assumption is used to estimate the bubble size from chordal distributions obtained by the optical probes discussed below).

The bubble size distributions were estimated by applying a non-parametric method based on the Parzen window estimator (Parzen, 1962). From a set of n measurements ($Y_1, Y_2, \ldots, Y_n$) of the experimental estimates of the major axis size, their pdf P, can be estimated as

$$P(y) = \frac{1}{nh\sqrt{2\pi}} \sum_{j=1}^{n} \mathrm{e}^{-(y-Y_j)^2/2h^2} \tag{1}$$

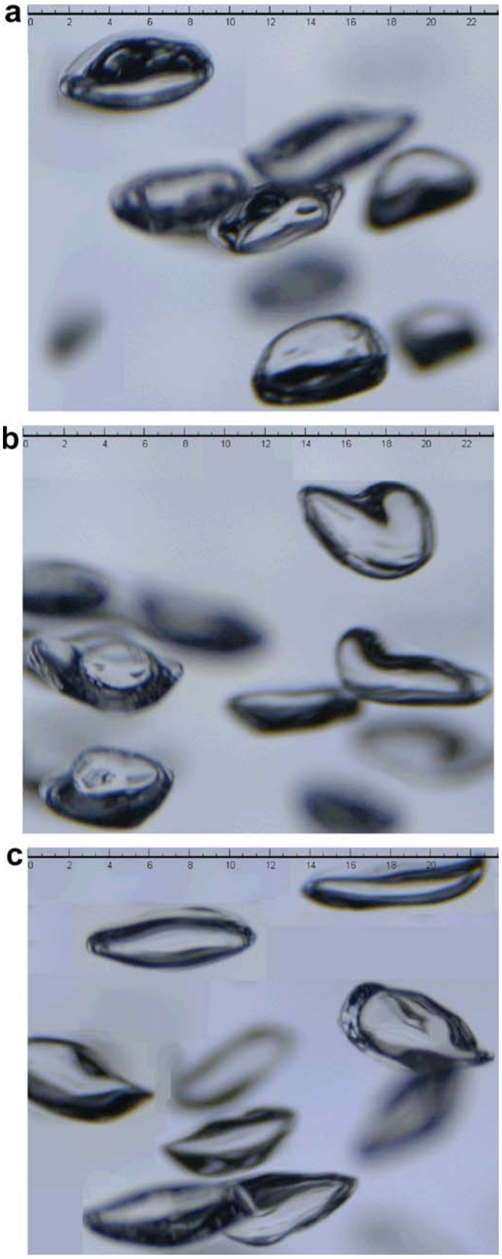

Fig. 3. Macro-photographic pictures of wobbling bubbles at 7.5 Nliter/min and an *average* void-fraction of about 0.5% (the superimposed rulers show centimeters).

where h is the Parzen window width. The optimal value of the Parzen window width can be determined by, for example, likelihood cross-validation, selecting the value that maximizes the leave-one-out log-likelihood:

$$\sum_{j=1}^{n} \log P_{Y_i}(Y_i, h) \tag{2}$$

where $P_{Y_i}(y, h)$ is the Parzen window pdf estimate constructed by leaving out Y_i.

The bubble size distributions were used to determine the interfacial area concentration, as discussed in the corresponding section below.

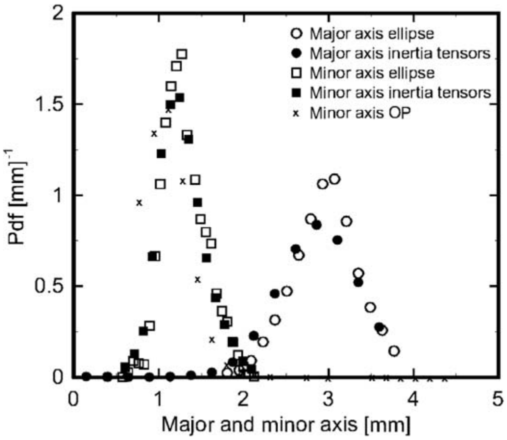

Fig. 4. Size distributions of the principal axes of the bubbles obtained by macro-photography and OP at 7.5 Nliter/min and a void-fraction of about 0.5%.

6. Double-tip optical probe technique

Five double-tip optical probes (OP), manufactured by the RBI company, were used to measure the characteristics of the gaseous phase, i.e., local void-fraction and bubble rise velocity (Cartellier and Achard, 1991; Wu and Ishii, 1999; Wu et al., 1999). A support system for the OP's, actuated by a stepping motor, allowed the radial scanning of the plume at different elevations from the injector. The OP's had a conical sapphire head of 500 μm diameter at its base with an angle of about 20°. The tips had a radius of about 50 μm, which guaranteed efficient piercing of the bubble interface. The comparison of the bubble velocities obtained by OP and PIV in the previous work of the same authors (Simiano et al., 2004) shows that the measurements agree within 3–10%.

6.1. Void-fraction measurements

The local void-fraction was obtained from (Cartellier and Achard, 1991; Wu and Ishii, 1999; Wu et al., 1999; Cartellier, 1990):

$$\alpha = \frac{\sum_i T_{G,i}}{T} \tag{3}$$

where $T_{G,i}$ are the gas presence times and T is the total duration of the measurement. Examples of void-fraction profiles plotted at several elevations from the top of the injector are shown in Fig. 5(a). The void-fraction measurements are always taken by the upstream tip of the sensors. Indeed, experimental observations have shown that the upstream tip had the tendency to repel bubbles away from the downstream tip. The error bars plotted on top of the void-fraction distributions represent the standard deviation of several consecutive series (17–20 series) of 2-min measurements.

The void-fraction close to the injector presents a flat profile with sharp boundaries; otherwise at higher elevations, the profiles became smoother and broader. The void-fraction measurements at higher elevations are shown in Fig. 5(b); these are normalized by the maximum void-fraction $\alpha_{\max}$ and with r_{HWHH}, the half width at half height (HWHH). The figure shows that the α profiles are reasonably distributed around a Gaussian fit in the developed-plume region.

The effect of the air flow rate on the void-fraction profiles is shown at two different positions in Fig. 6, very close to the injector, Fig. 6(a), and further up, Fig. 6(b). The irregularities, present for all the flow rates, at about $X = -15$ mm are due to two bent injector needles.

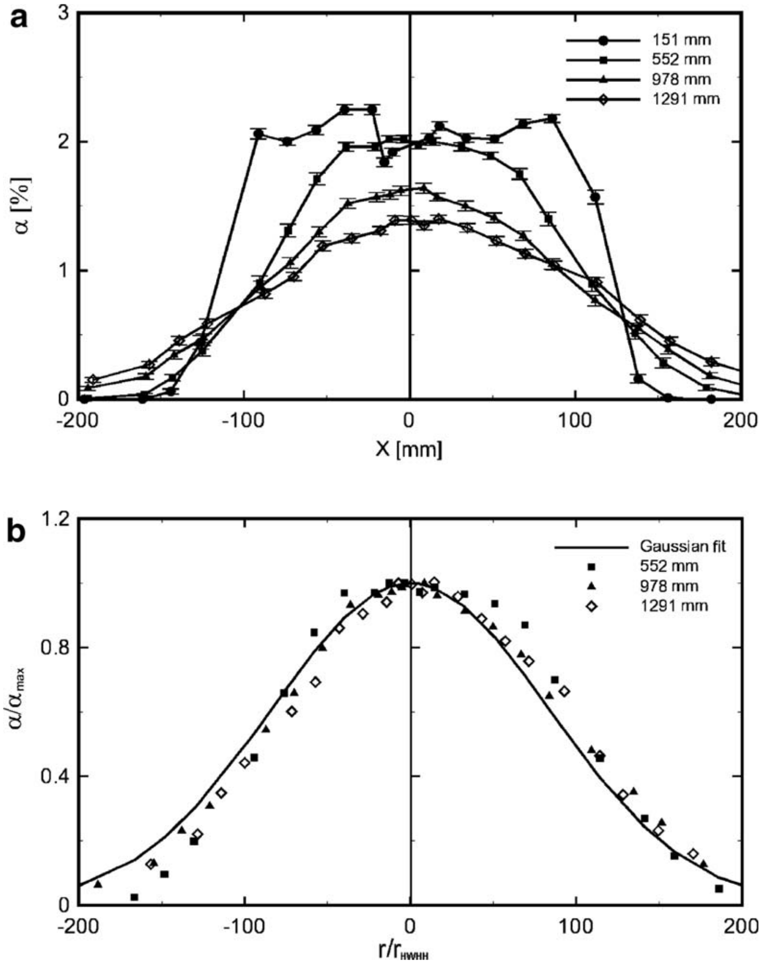

Fig. 5. Time-averaged void-fraction profiles at different elevations above the injector at 30 Nliter/min. (a) Void-fraction profile at all elevations. (b) Best fit of normalized profile at the higher elevations.

6.2. Mean bubble diameter and interfacial area concentration

The macro-photographic images, Fig. 3, and the bubble size distributions, Fig. 4, show that the actual bubble shape is not spherical and that an ellipsoidal shape is a reasonable approximation for the real "wobbling" bubbles. Following Liu and Clark (1995) and Liu et al. (1998), we assume an ellipsoidal shape with rotational symmetry around the vertical axis. The principal axes of the ellipsoid are denoted by $2R$ (major) and $2eR$ (minor), e being a shape factor which was assumed constant and estimated from an analysis of the macro-photographs; the average value of e was found to be 0.515. Liu and Clark (1995) and Liu et al. (1998) derive the bubble size distribution from the measured chord length distribution using a statistical approach (uniform spatial probability of piercing the bubble):

$$M_{\mathrm{CL}} = \frac{4e}{3} M_{2R} \tag{4}$$

where M_{CL} and M_{2R} are the mean of the distributions of the chord length and of the major axis size, respectively.

An interesting comparison between the bubble size distributions obtained by processing of the macro-photographic images and by the optical probes is reported in Fig. 4. The experimental estimations are in fair agreement, validating once more the use of the assumption of ellipsoidal bubble shape, necessary to extract the

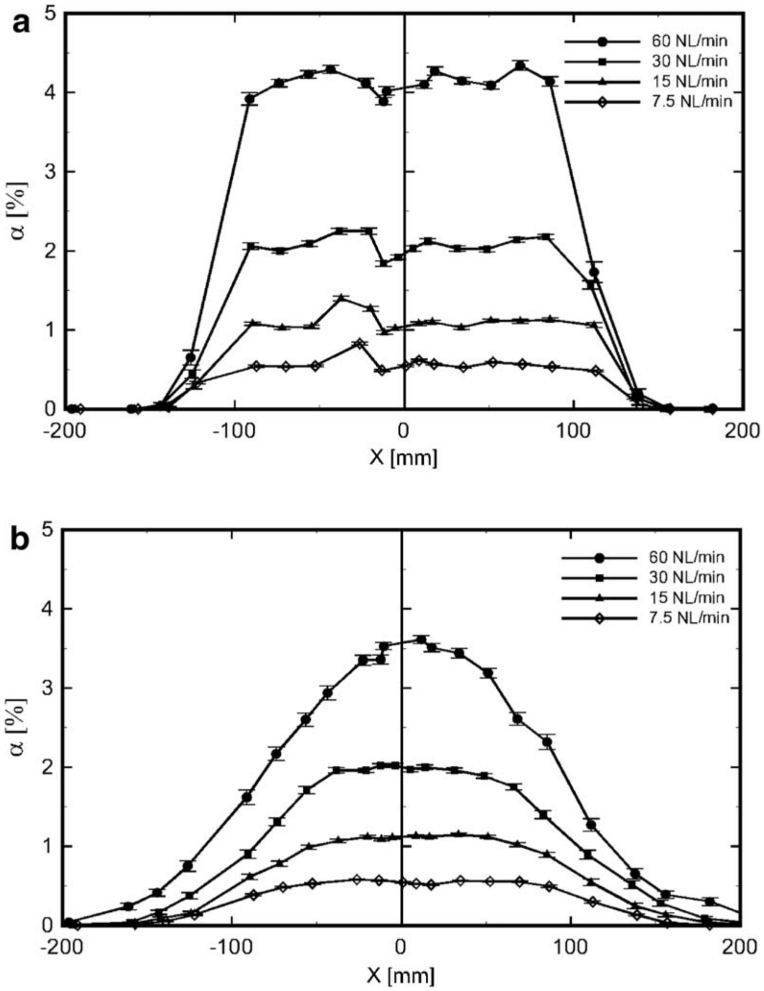

Fig. 6. Time-averaged void-fraction profiles as function of the gas injection rate at two elevations: (a) 151 mm and (b) 552 mm.

bubble size from the chord length distributions obtained with the OP technique. Further details of this study can be found in the previous work of Zboray et al. (2004). Bubble major axes obtained with Eq. (4) from the measured mean chord lengths M_{CL} are presented in Fig. 7(a) as function of the elevation and in Fig. 7(b) as a function of the injection rate. The error bars represent the standard deviation of all the measurements at a given point from the mean.

Fig. 7(a) shows a weak monotonous trend except for the bubble size at elevation 552 mm which is always lower then at other elevations. A fraction of the observed growth of the bubbles with elevation can be attributed to the reduced hydrostatic pressure (2–4% in radius). The remaining apparent growth may be due to unlikely coalescence, changes in shape with elevation or to the measurement accuracy, like slight differences between the different OPs, slight differences in the vertical alignment of the probe tips, etc.

The variation of the bubble size with the gas flow rate, Fig. 7(b), is a dynamic effect of bubble formation. The bubble size at the injector needles, at the limit of infinitely slow bubble formation, can be determined by equating the buoyancy force acting on the bubble with the surface tension force along the needle perimeter. This bubble size would be independent of the gas injection flow rate. For higher injection flows, as in the present work, however, bubble formation cannot be considered to be stationary and the bubble size increases with the injection flow rate, as the bubbles take a finite time to break from the orifice. Estimating this time, for orifices with constant flow rate, Davidson and Harrison (1963) give a correlation for the bubble volume at detachment that agrees well with our experimental data.

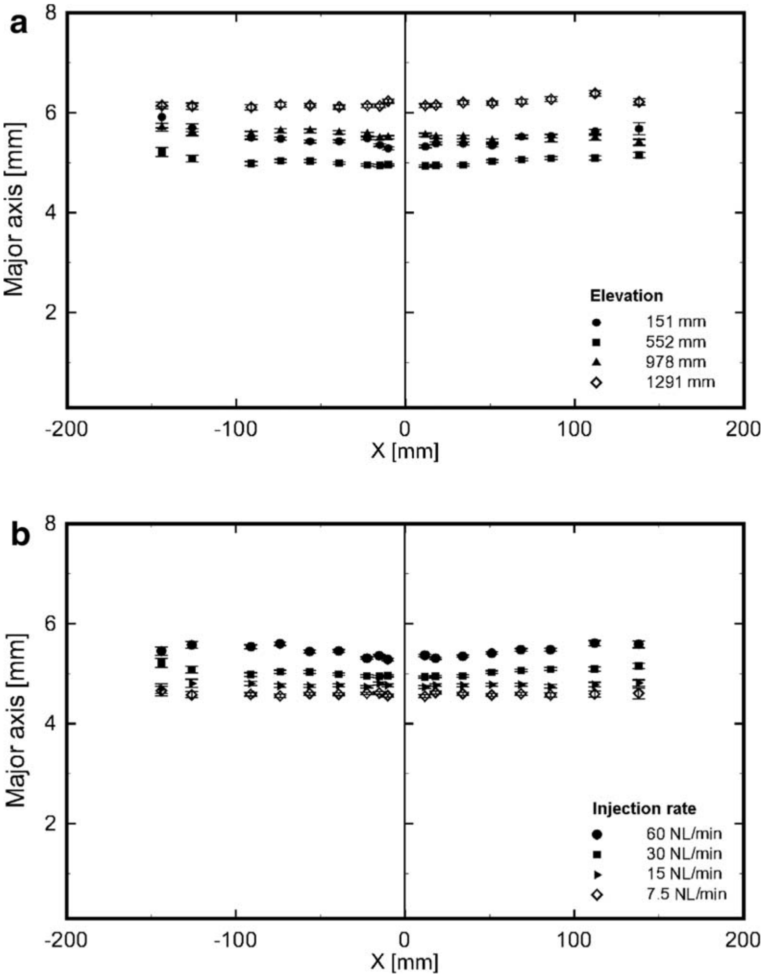

Fig. 7. Influence of the elevation and of the gas flow rate on the size of the major axes of the bubbles. (a) Effect of elevation at the injection rate of 30 Nliter/min. (b) Effect of injection rate at the 552 mm elevation.

Fig. 7 also shows that the mean bubble size profile remains practically radially flat. Moreover, as detailed examinations show, the distribution of the measured chord lengths is practically the same at different radial positions of the plume. This shows that the injector is indeed producing monodisperse bubbles and that there is no spatial separation of the bubbles according to any slight differences in their size, due, e.g., to the change of the sign of the lift force for bubbles above ≅5.8 mm, as shown by Tomiyama (1998).

The radial distribution of the interfacial concentration follows that of the void-fraction. Its values are determined by taking into account the bubble size distribution. Details and results are given by Zboray et al. (2004).

7. Global plume dynamics by image processing of the PIV pictures

PIV pictures can be used to delineate the instantaneous position and limits of the plume in the observation plane. Each PIV picture shows a vertical cross-section of the bubble plume. Due to the fluctuations, the centre of the plume cross-section in a horizontal plane may be outside the vertical laser sheet plane. Thus, the centreline position represents the situation on the observation plane only, and the *apparent* plume diameter is in fact a chord length.

Depending on injector size, air-flow rate and immersion depth, bubble plumes may have strong fluctuations around their nominal axis (Rensen and Roig, 2001; Mudde et al., 1997). At lower immersion depths, our plumes reached a steady but asymmetric configuration. In our experiments, the fluctuations increased with immersion depth and/or the injection rate. The oscillatory behaviour could be well-observed visually, consisting of an apparently stochastic motion of the whole plume around its axis, with plume width and horizontal cross-section fluctuations increasing with distance from the injector. At the plume border, the fluctuations produce a wavy motion of the vertical plume edge, which was also observed in 2D bubble plumes (Rensen and Roig, 2001). Consecutive instantaneous velocity fields show clusters of higher-velocity bubbles travelling up in the plume. The inside of the plume can be quite inhomogeneous as a result of dispersive, turbulent effects and clustering of the bubbles. Another effect that distorts the plume shape is that a few bubbles may be dispersed around it. It should be emphasized that the bubble plume dynamics is intrinsically three-dimensional, whereas only 2D information is available from our vertical plane PIV pictures. The *apparent* plume cross-sections do not allow a full description of the phenomena, nevertheless, important insights can be drawn.

An ad hoc Matlab routine was written to detect the contours of the *apparent* plume vertical cross-section appearing in the laser sheet. The images, as in Fig. 2(a), are initially enhanced by removing the background luminance. Afterwards, the picture is converted into a binary image by using a threshold value which was determined by trial and error. The result is a black and white image where the bubbles consist of white pixels. A *dilatation* and a *filling* operation are applied to improve the quality of the bubble images transforming them into filled objects. The picture is then subdivided into small square interrogation areas of roughly the bubble size (5 × 5 mm). For each interrogation area, the number of white pixels is estimated. The bubble plume region was defined as the row of horizontal interrogation areas which contained 95% of the white pixels; so that the two extreme squares represent the contour positions. This approach avoided the problem arising from a single bubble, displaced away from the bubble plume, biasing the contour position estimation. The "*centreline*" in this plane is the locus of middle points between left and right contours. Statistical studies were carried using this information.

A spectral analysis was carried out for the axis movement at several air flow rates, in order to investigate the plume oscillation. The main oscillation modes were at low frequencies, (of the order of 0.01 Hz and above), as Fig. 8 shows. The plume meandering frequency increases linearly with increasing injection rates, Fig. 9, which

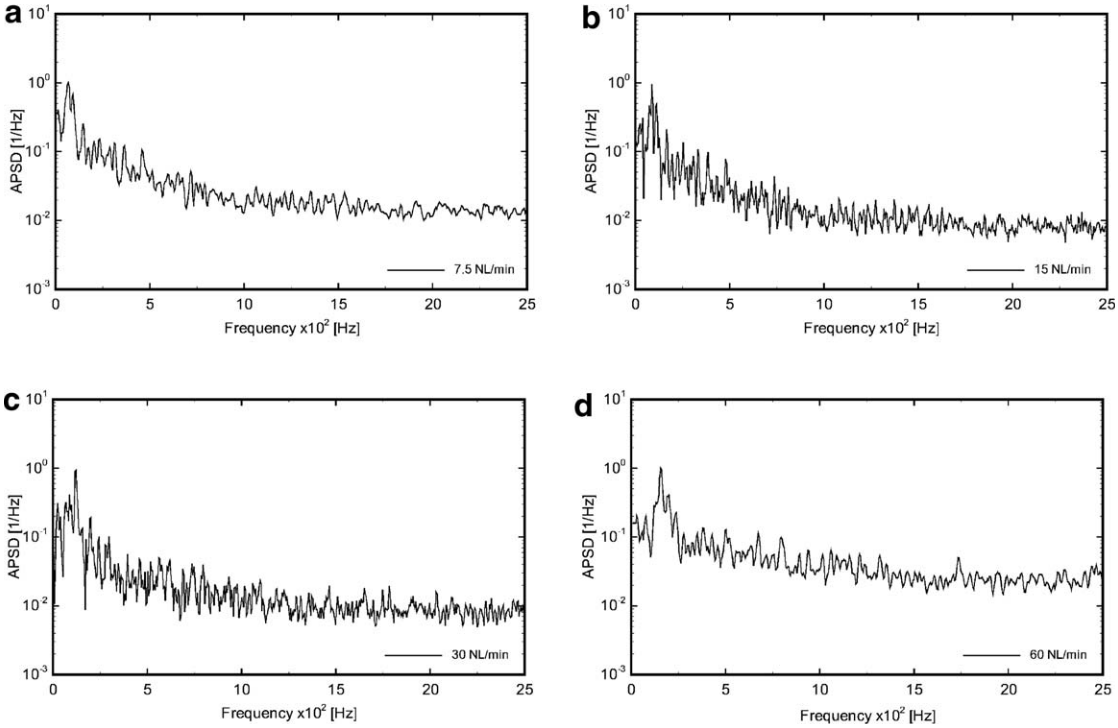

Fig. 8. Frequency spectrum of the *apparent* plume centre position for several air flow rates. (a) 7.5 Nliter/min, (b) 15 Nliter/min, (c) 30 Nliter/min and (d) 60 Nliter/min.

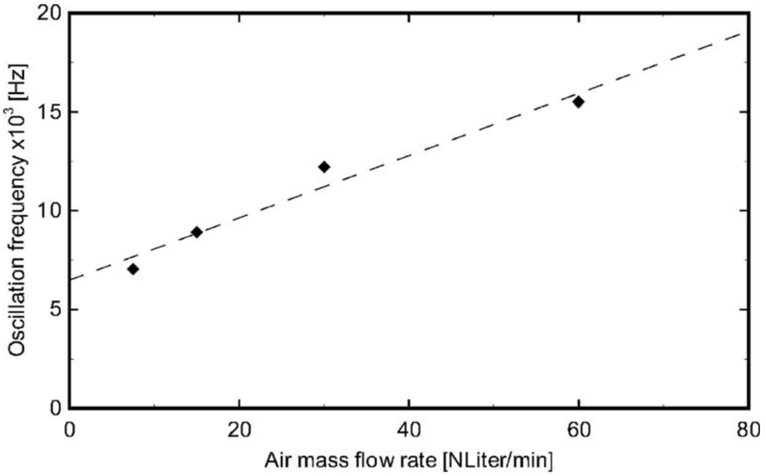

Fig. 9. Main mode frequency of the *apparent* plume centre position as function of the air flow rate.

is in qualitative agreement with the findings by Rensen and Roig (2001) for a 2D bubble plume. Again in accordance with Rensen and Roig (2001), it was found that, for a given injection rate, the oscillation frequency practically does not change with elevation in the plume.

The apparent centreline position and apparent plume diameter pdf (obtained with the non-parametric method based on the Parzen window estimator) are shown in Figs. 10 and 11. Fig. 10 shows a clear increase of the scatter of the instantaneous position of the plume centreline between elevations 250 mm and 600 mm, but no significant further spread above 600 mm. This saturation effect, also reported by Rensen and Roig (2001) for 2D bubble plumes, was explained by the wall confinement effect, since in their case the bubble plume edges were very close to the tank wall. However, in our experiments, the bubble plume borders are still far away from the vessel wall, therefore this explanation is not reliable. The instability of the bubble plume structure is clearly coupled with the large-scale eddies which, created at the plume boundaries, travel upwards. This

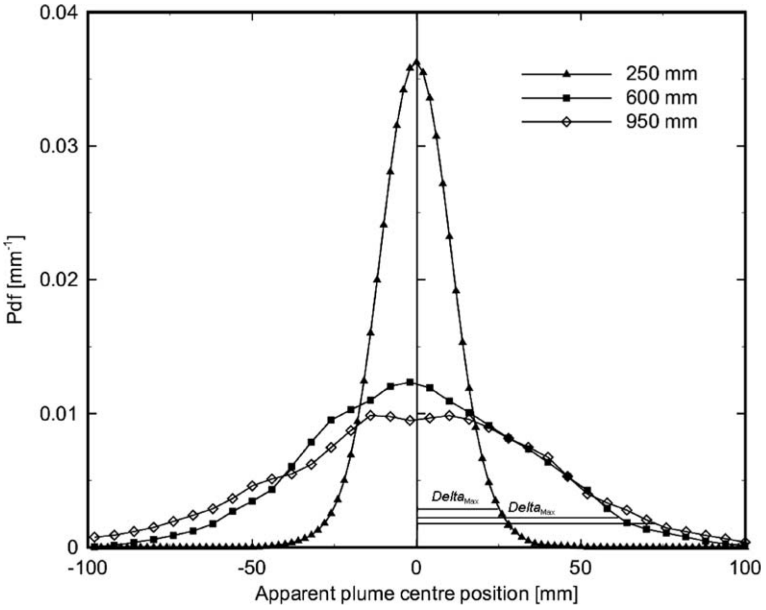

Fig. 10. Experimental distribution of the *apparent* plume centreline position at three elevations at 30 Nliter/min.

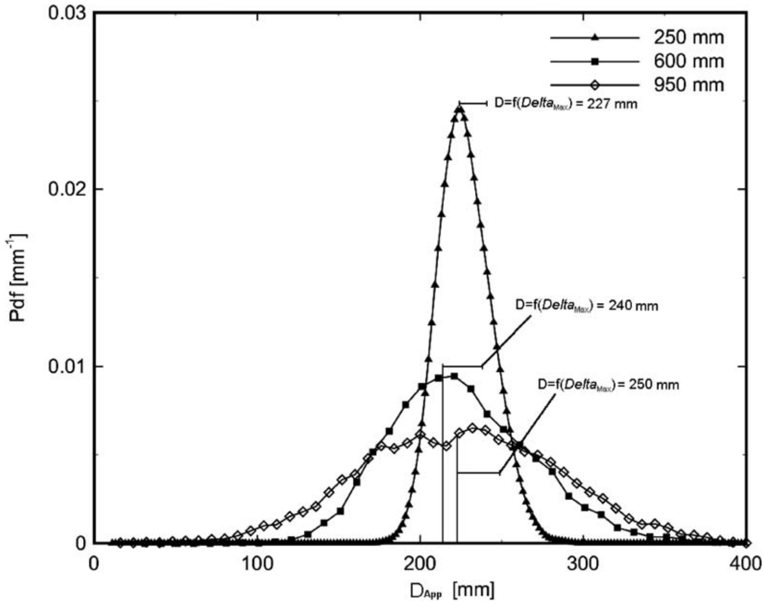

Fig. 11. Experimental distribution of the *apparent* plume diameter at three elevations at 30 Nliter/min.

phenomenon was modelled for single-phase turbulent buoyant plumes by Bejan (1982). Those large eddies, coupled with the vorticity due mainly to the transversal gradient of the liquid velocity, are also partially responsible for the entrainment needed to supply the spreading of the liquid velocity profile. At elevations below 600 mm, as shown in Section 8.2, the liquid is still accelerating upwards, producing vorticity which supplies the eddies. Higher up, the flow becomes fully developed presenting a plateau of the liquid velocity. Moreover, the radial velocity, which was inward, decreases and, approaching the free surface, becomes outward (for details see Simiano (2005)), destroying and shifting the remaining large eddies. This might explain the saturation effect of the plume position oscillation at high elevation.

In Fig. 11, the pdf of the apparent plume diameter, D_{App}, is plotted for three elevations. Due to the meandering, the measured *apparent* diameter is actually a chord of the bubble plume horizontal cross-section, as already mentioned, and therefore always smaller than the real diameter. An estimation of the maximum error, due to the out-the-PIV-plane displacement of the plume axis, is given assuming the following: the instantaneous horizontal cross-section of the bubble plume is circular; the distribution of the out-of-plane displacement of the centreline position is equivalent to what is shown in Fig. 10 for the in-the-PIV-plane scatter. The first hypothesis is the simplest one allowing to correlate D_{App} with the real diameter D, the second is confirmed by independent measurements obtained with different camera-to-laser orientation. From the pdf of the centreline position, Fig. 10, a maximum out-of-plane centreline displacement $\text{Delta}_{\max}$ can be defined as the centreline displacement which includes at least 95% of the occurrences. By assuming an instantaneous circular horizontal cross-section, D, it can be expressed as $D = 2\sqrt{(\text{Delta}_{\max})^2 + \left(\frac{D_{\text{App}}}{2}\right)^2}$. Therefore, for each D_{App} in Fig. 11, the real diameter D will have a value between D_{App}, in case of nil out-of-plane displacement, and $D = f(\text{Delta}_{\max})$ given by the expression above for a $\text{Delta}_{\max}$ displacement.

The apparent diameter distribution at 250 mm above the injector, Fig. 11, showed a mode (the most probable value of the distribution) at 220 mm, which would lead to a real diameter in the range $220\text{ mm} < D < 224\text{ mm}$ for a $\text{Delta}_{\max}$ of about 20 mm. These diameter D results are smaller than the injector diameter of 300 mm. In fact, visual observation of the plume revealed that a strong contraction occurs just above the injector. At higher elevations, 600 and 950 mm in Fig. 11, the pdf became broader and larger than at the lower elevation. Moreover, the means of these pdfs refer to a plume diameter D in the ranges of about 210–240 mm and 220–250 mm with a $\text{Delta}_{\max}$ of about 60 and 65 mm, respectively. The wider distributions at higher elevation are due to the larger plume width oscillation and to the 3D plume structure motion previously described, which appear as a fluctuation of the apparent plume diameter. Therefore, at about two-thirds of the total plume height, the 950 mm elevation in Fig. 11, the pdf of the apparent plume diameter shows also a saturation effect similar to that of the centreline plume position.

Previous investigators of bubble plumes (Milgram, 1983; Fannelop et al., 1991; Kobus, 1968) observed an increase of the width of the time-averaged profiles with elevation. For the liquid velocity fields, Kobus (1968) defined b as the rate of spread, by interpolating the liquid velocity profiles with a Gaussian curve such as $\bar{\bar{v}}_L = \bar{\bar{v}}_{L0} \cdot \mathrm{e}^{\frac{-r^2}{b^2}}$. Instead, our results refer to the spreading of the instantaneous core of the bubble plume, measured by looking at the instantaneous apparent pictures. The observations proved that, at any instant, there is little plume spreading in our experiment, although the measured time-averaged velocity and void-fraction profiles show much greater broadening at higher elevations. In fact, it is the meandering, the oscillation of the axis of the plume, that makes the time-averaged profiles significantly flatter and broader at higher elevations rather than an instantaneous spreading of the bubble plume core. Following the same reasoning, the Gaussian spreading presented by the time-averaged void-fraction profile, Fig. 5(b), has also to be interpreted in relation to the bubble plume structure instabilities. In fact, the evolution of the time-averaged void-fraction profiles from top-hat close to the injector, to a Gaussian distribution further up, is not only due to the turbulent diffusion and lift forces acting on the bubbles but also to the strong global bubble plume meandering which affects significantly the time-averaged profile.

8. PIV results

Prior to presenting and analyzing the PIV velocity fields, some considerations have to be made about the information contained in these measurements in relation to the data analysis technique.

The two-frame cross-correlation PIV is based on two pictures taken with a short delay in time. As the velocity field is extracted in each IR by cross-correlation, each velocity vector is a spatially weighted average of the time-averaged velocity field in one IR. In this respect, it must be stressed that the velocities from PIV measurements are different in nature from velocities obtained by a single-point velocimetry technique.

The PIV technique inherently applies a spatial low-pass filter (with a top hat window) to the data, and therefore care must be taken when statistical quantities such as time-averaged mean velocities and stress terms are extracted from such PIV data.

A true instantaneous velocity φ_j can be decomposed as

$$\varphi_j = \tilde{\varphi}_j + \varphi_{\text{unresolved}}$$

where $\tilde{\varphi}_j$ is the experimentally resolved velocity obtained with the PIV space averaging, and $\varphi_{\text{unresolved}}$ is the unresolved velocity component that was filtered out by the intrinsic filtering. The delay between two PIV pulses varied, according to the velocity to be measured, within a range of 2–4 ms, which is several times larger than the integral time scale of the flow. Therefore $\varphi_{\text{unresolved}}$ will have also some contributions from the time filter introduced by the PIV technique. The PIV time filter can be considered as an integral filter, defined as

$$\tilde{\varphi}_j = \frac{1}{\Delta t}\int_0^{\Delta t} \varphi_j \cdot \mathrm{d}t \tag{5}$$

where Δt is the time delay between the two PIV frames. The frequency response of such a time filter is given by

$$H(jw) = \frac{1 - \mathrm{e}^{-\mathrm{j}w\Delta t}}{\mathrm{j}w\Delta t} \tag{6}$$

For a constant signal, $w = 0$, the module of the frequency (w) response $\|H(w)\|$ is equal to 1; higher frequencies will be instead attenuated. Knowing the Δt, the attenuation coefficient can be estimated as function of the frequency. An estimation of the attenuation coefficient will be given later.

The instantaneous experimentally resolved velocity $\tilde{\varphi}_j$ can be again decomposed as

$$\tilde{\varphi}_j = \overline{\tilde{\varphi}_j} + \tilde{\varphi}_j{}' \tag{7}$$

where $\overline{\tilde{\varphi}_j}$ is the time-averaged and $\tilde{\varphi}_j{}'$ is the fluctuating part from such a decomposition, time-averaged stress terms can be derived as

$$\overline{\tilde{\varphi}_j{}'\tilde{\varphi}_i{}'} = \frac{1}{M-1}\sum_{k=1}^{M}[(\tilde{\varphi}_j - \overline{\tilde{\varphi}_j})(\tilde{\varphi}_i - \overline{\tilde{\varphi}_i})] \tag{8}$$

where M is the total number of samples collected during the measuring time.

8.1. Bubble velocity fields

An example of a vector plot showing the average bubble velocity field is presented in Fig. 12(a). This average velocity vector field is obtained by superposition of many instantaneous fields, similar to the one shown in

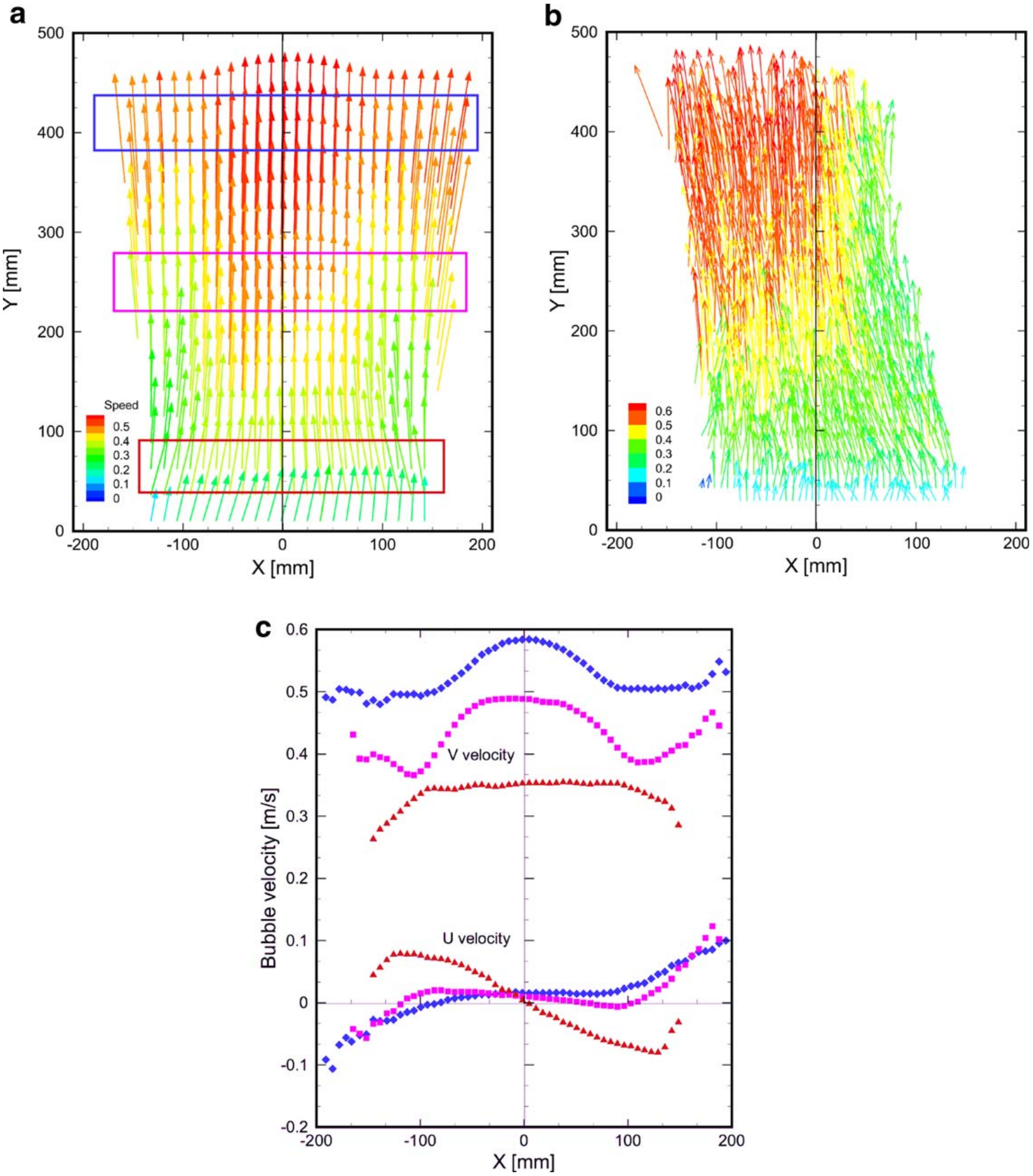

Fig. 12. Bubble velocity fields and velocity profiles at the injection rate of 30 Nliter/min. (a) Time-averaged field, (b) Instantaneous field and (c) time-avaraged profiles at three elevations: (▲) $Y = 60$ mm, (■) $Y = 250$ mm, (◆) Y = 420 mm.

Fig. 12(b). Time-averaged velocity profiles were obtained from the average velocity field of Fig. 12(a). A velocity vector was placed at the centre of each IR and each profile was further averaged over four successive horizontal rows of IR's. The size of the resulting spatial filter was therefore 24 × 6 mm.

In Fig. 12(c), the vertical (V) and horizontal (U) components of the average velocity profile are displayed for the three different levels of the plume investigated that correspond to the rectangles added to Fig. 12(a). Close to the injector, the vertical (V) velocity component shows a very flat profile, while at higher elevation it evolves, reaching a higher centreline velocity and a smoother edge. The profile of the horizontal component at $Y = 60$ mm is due to the contraction of the plume; the horizontal component at the plume periphery has an inward direction. The convention used to display the profiles is that positive directions are the upward and rightward directions; this explains the sign of the velocities. At the lowest elevation, the velocity is inward because of the contraction of the plume.

A comparison of the time-average bubble velocity profiles at the 600 mm elevation above the injector is shown in Fig. 13, for three different gas injection flow rates. As indicated previously, the larger the air mass flow rate, the stronger the plume oscillations, and this is reflected in the spreading of the average velocity profiles. Stronger plume oscillations made the velocity profile broader and flatter. We may note here that the evident role of the oscillations in spreading the plume in time-averaged plots, makes the interpretation of any time-averaged computational results challenging: in fact, although computed average profiles may match the experimental ones, there is no guarantee that computations also match the instantaneous profiles and consequently do not unambiguously qualify the closure laws used in the computations.

The averaged injector-centreline bubble velocities and their fluctuations are plotted in Fig. 14 along the plume height, for three different gas flow rates. The whole height is investigated through the three available facility windows, shown in Fig. 1. The three investigated regions do not overlap, which explains the two gaps without measurements in Fig. 14. It was already reported that the PIV measurements are quite sensitive to the laser light attenuation due to bubble reflections. In addition, another source of bias is the vertical spreading and attenuation of the laser sheet along the area investigated, also affecting the accuracy of the results and explaining the small discontinuities about the gaps.

Three zones can be observed, independently from the flow rate. The first zone exhibits steeper slopes for higher flow rates, the second, instead, is characterized by roughly the same slopes. In the upper zone, above 800 mm, the flow can be considered fully developed since the centreline mean velocity is roughly constant.

8.2. Liquid velocity fields

The liquid velocity estimation was made difficult by the attenuation of the laser light by the bubbles, as stated above. The liquid velocity profiles obtained by averaging several instantaneous liquid velocity fields

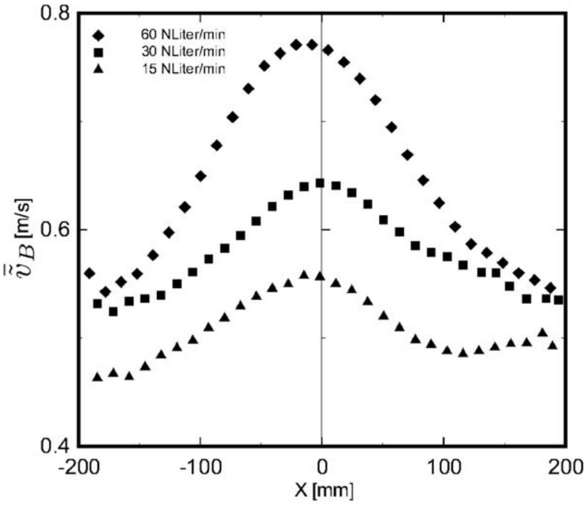

Fig. 13. Time-averaged bubble velocity profiles for three different air flow rates at the elevation of 600 mm.

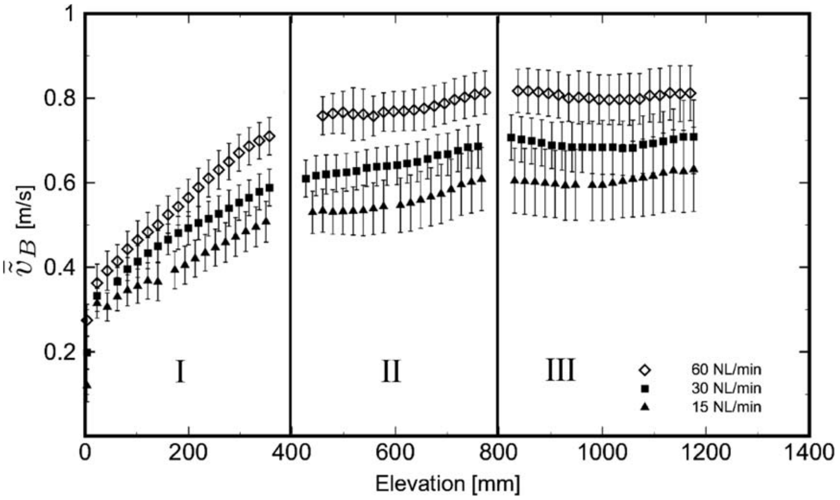

Fig. 14. Time-averaged injector-centreline bubble velocity at three different air flow rates.

and mirrored to the centreline axis, are plotted in Fig. 15 for the 600 mm elevation. It is important to recall that the liquid- and the bubble-velocity fields are not obtained simultaneously and therefore the true instantaneous relative velocity cannot be determined and averaged to obtain the average relative velocity. Simultaneous measurements require a second camera that was not available at this phase of the work. Subtracting the average phase velocities to derive the average relative velocity is in principle incorrect since the measurements are not statistically independent; for this reason this is not attempted here.

In Fig. 16(a) the injector-centreline liquid velocity is plotted against the plume elevation for three different air flow rates. Again, the measurements could be performed only in limited regions of the plume height where the three windows were located, but in narrower zones, corresponding to the narrower laser beam sheet. The results suggest that the injector-centreline liquid velocity becomes constant above a certain elevation, which corresponds to the zone where the flow can be considered fully developed, Fig. 14.

Two components of the time-averaged stress tensor of the liquid are plotted in Fig. 16(b), as function of the plume elevation, for the 15 Nliter/min gas flow rate. The figure shows the stress terms to increase with elevation, even above 600 mm, where the mean centreline liquid velocity does not change anymore. This behaviour

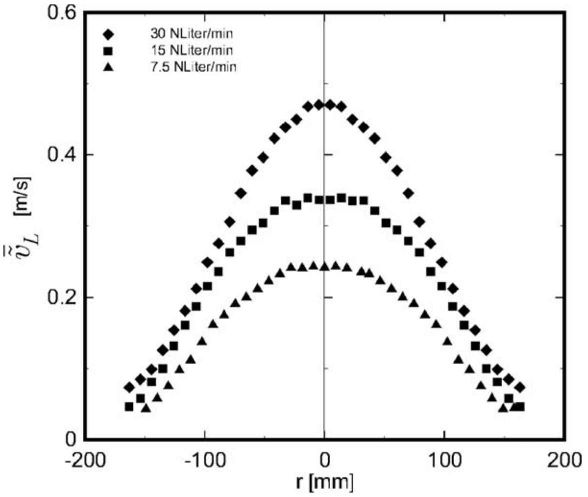

Fig. 15. Liquid velocity profiles for three different gas flow rates at the elevation of 600 mm.

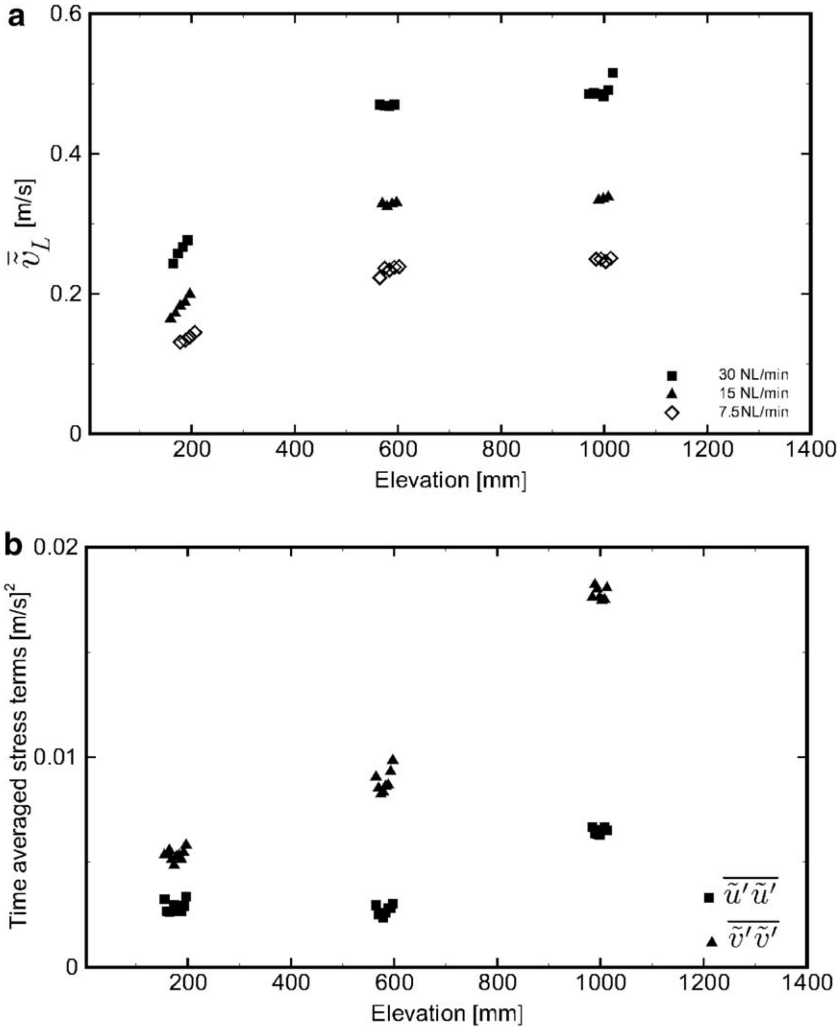

Fig. 16. Time-averaged injector-centreline velocity at different air flow rates and stress profiles of the liquid phase. (a) Mean filtered term $\overline{\tilde{v}}_L$. (b) Time-averaged stress terms $\overline{\tilde{v}'\tilde{v}'}$, $\overline{\tilde{u}'\tilde{u}'}$ for 15 Nliter/min.

maybe due to the increasing plume instability, which leads to higher velocity fluctuations. Moreover the increase is more substantial for the $\overline{\tilde{v}'\tilde{v}'}$ terms, which leads to the conclusion that the anisotropy of the turbulence is clearly more pronounced in the fully developed area.

The velocity fluctuations result from coupled gas–liquid interaction mechanisms including: the random stirring of the continuous phase by the motion of the dispersed phase, vortex shedding in the wakes of the bubbles, and the large-scale coherent structures superimposed on the plume oscillation mode. Therefore, it is possible to have a rough idea of the frequency range for kinetic energy production. In bubble plumes, there are two primary length scales associated with turbulence production, namely the plume width and the bubble diameter. A typical frequency of turbulent eddy production in the bubble wake can be estimated by the ratio between the relative velocity (○)10^{-1} m/s and the bubble diameter (○)10^{-3} m, i.e. about 100 Hz. For large-scale eddies in the plume, a typical frequency can be estimated as the ratio between the plume liquid velocity (○)10^{-1} m/s and the plume width (○)10^{-1} m, i.e. about 1 Hz (Sjoen, 1983). Due to the lack of time resolution beyond the 15 Hz data acquisition rate, it was not possible to discriminate which part of the spectrum contributes to the energy production. Moreover, the time filter introduced by the PIV due to the delay between the two laser pulses also biases the results, as it has a frequency response similar to that of an integrator filter, as shown in Eq. (6). For a laser pulse delay of 2 ms, a signal with a frequency of 100 Hz (typical turbulent eddy frequency for our flow) will have a frequency response of about 0.94; instead, for a pulse delay of 4 ms the frequency response will be about 0.76. Thus, despite the inherent PIV time filter, the energy related to the most important frequencies of our flow will be measured with a slight attenuation only. Therefore, the stress terms reported here still contain the main contributions from the turbulent production frequencies.

In Fig. 17(a), (c) and (e), cross-sectional profiles of all available stress terms are plotted for different gas flow rates. All of them can be scaled with the void-fraction in the range of $0.5\% < \alpha < 2.5\%$, as shown in the corresponding Fig. 17(b), (d) and (f). Generally, linear scaling of the turbulent fluctuations with the buoyancy term is not unexpected and can be found in single-phase buoyant plumes. George et al. (1977), for example, providing self-similarity correlations, linked the buoyant term $-g\frac{\Delta\rho}{\rho_\infty}$ to the square of the mean stream velocity fluctuations with a linear relation using a buoyant-source parameter. In bubble flows instead, a linear scalability with the void-fraction was reported by other authors. Wijngaarden (1982) derived the bubble-induced

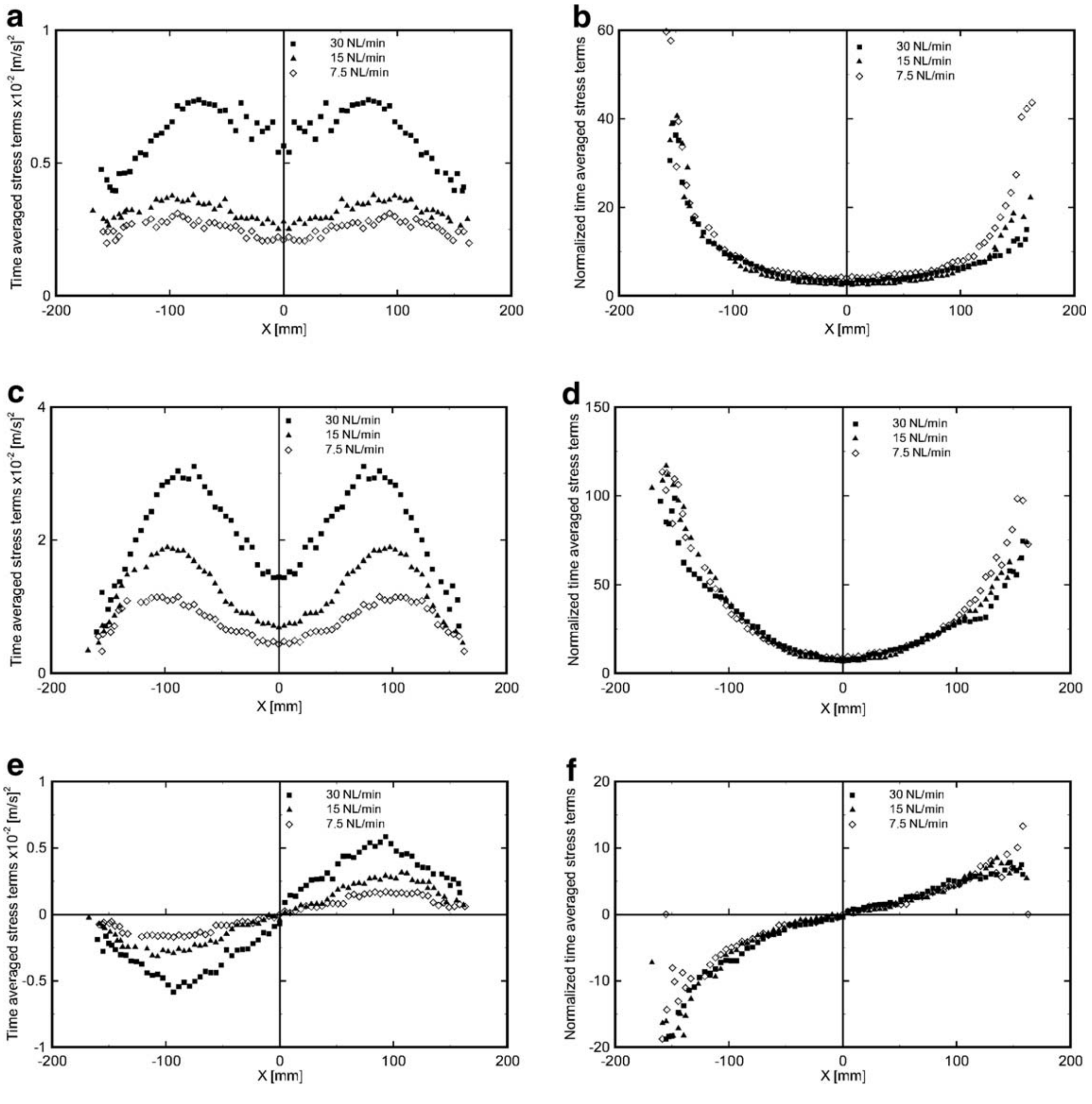

Fig. 17. Horizontal time-averaged stress profiles of the liquid phase for three different air flow rates at the 600 mm elevation. (a) Stress terms $\overline{\tilde{u}'\tilde{u}'}$, (b) normalized stress terms $\overline{\tilde{u}'\tilde{u}'}/(\alpha U_R^2)$, (c) stress term $\overline{\tilde{v}'\tilde{v}'}$, (d) normalized stress terms $\overline{\tilde{v}'\tilde{v}'}/(\alpha U_R^2)$, (e) stress terms $\overline{\tilde{u}'\tilde{v}'}$ and (f) normalized stress terms $\overline{\tilde{u}'\tilde{v}'}/(\alpha U_R^2)$.

fluctuating kinetic energy for potential flow with the assumption of identical spherical bubbles. Lance and Bataille (1991) found the liquid velocity normal fluctuations to scale linearly with α, for $\alpha < \alpha_c = 10^{-2}$. Otherwise, at higher α, larger velocity fluctuations and disturbed bubble trajectories were observed which translated into a non-linear scaling of the liquid-phase stresses with α. Increasing void-fraction is synonymous to strong interaction between neighboring bubble wakes, explaining the zig-zag motion of the bubbles. Further, by getting closer to each other (increasing α), the bubbles do not remain spherical and that changes the form of the expression of the liquid kinetic energy induced by spherical bubbles in quiescent fluid (Biesheuvel and Wijngaarden, 1984; van Wijngaarden, 1998).

Climent and Magnaudet (1999) also found a similar linearity, carrying out a large-scale simulation of bubble-induced convection in a liquid layer. By analogy to thermal convection, they defined two flow regimes as function of the Rayleigh number, keeping constant the Prandtl number $Pr_0 = 2.5 \times 10^{-4}$. For $Ra < Ra_c = 2.0 \times 10^5$, where Ra_c corresponds to their Pr_0, the liquid velocity fluctuation was smaller than the terminal bubble velocity U_R and grew linearly with the void-fraction. Larger velocity fluctuation and strong instabilities of the flow pattern were instead obtained for $Ra > Ra_c(Pr_0)$. In our experiments, the Rayleigh number, in the range of $3.4 \times 10^5 < Ra < 2 \times 10^6$, is larger than Ra_c reported in their simulations, but for a much larger Prandtl number ($Pr = 2.2$). This suggests that it is difficult to extent their criteria to the present work.

Risso and Ellingsen (2002), investigating a homogenous bubble flow with a void-fraction range of $0.5\% < \alpha < 1.05\%$, and an equivalent bubble diameter of 2.5 mm, found two regions of interest. In the vicinity of the bubble, the flow had strong similarity to that of the single rising bubble with a potential-flow characteristic in front and controlled by the wake behind the bubble. Far from the bubble, the liquid velocity fluctuation was characterized by a non-linear interaction of the bubble wakes and therefore scaled with $\alpha^{0.4}$.

The results reported here, cannot bring a clear understanding of the role of the bubble wake since the PIV velocity measurements were obtained by applying a cross-correlation in an IR of 4.6×4.6 mm. This correlation introduced a spatial-low-pass filter similar to the time filter described in Section 8. Following the same approach, the frequency response of the spatial filter can be derived. Fluctuating structures with a length scale smaller that $\approx$5 mm are practically filtered out; structures with length scales of 7, 8, 9 mm have an attenuation of 0.43, 0.54, 0.62, respectively. This means that in our PIV results, scales smaller than $\approx$10 mm, were conspicuously attenuated.

Finally, it can be concluded that at least the "mesoscopic" scale structure, with length scales intermediate between bubble diameter and typical size of the large-scale structure of the flow, contribute (in the range of $0.5\% < \alpha < 2.5\%$) with a linear relation to the void-fraction, as also found by Climent and Magnaudet (1999).

9. Conclusions

An extensive experimental campaign has been carried out with fairly large-scale bubble plumes in the LINX facility. The measurements have been performed under well-defined injection conditions and the gas injection flow rate has been systematically varied in the tests. Void-fraction, liquid and bubble velocities and bubble-size distributions have been obtained inside the plume using a variety of measurement techniques. The experimental data have been processed using advanced methods.

This work provided instantaneous liquid and gas velocity fields and averaged void-fraction data. Statistical studies were performed using image processing to determine the diameter, the instantaneous centreline position distributions of the bubble plume core and their fluctuations in time. An important finding was that there is not much *instantaneous* spreading of the bubble plume core and that the measured average spreading is mainly due to the meandering and oscillations of the plume. The frequency of the plume oscillation was found to be linearly increasing with the air flow rate.

Stress tensor terms were obtained from the instantaneous velocity data. For the continuous phase, a linear scalability of these terms with the void-fraction was shown in the range of our experiments $\alpha = 0.5$–2.5%; where the main measured contributions to the fluctuations come from length scales larger than the bubble size.

The time-dependent and instantaneous measurements database collected in these experiments forms a valuable and consistent dataset for the validation and development of advanced three-dimensional two-phase flow simulation tools.

Acknowledgements

The authors gratefully acknowledge support from the Emil Berthele Fonds (ETHZ). Part of this work has been carried out within the ASTAR project of the 5th Euratom Framework Programme Nuclear Fission, with financial support from the Swiss Federal Office for Education and Science under contract No. 99.0796. This support is also gratefully acknowledged.

References

Adrian, R.J., 1991. Particle-imaging techniques for experimental fluid mechanics. Annu. Rev. Fluid Mech 23, 261–304.

Arnold, H., Yadigaroglu, G., Gonzales, A., Rao, A.S., 1997. An economic passive plant design. Jahrestagung Kerntechnik 97. Aachen, Germany.

Bejan, A., 1982. Theory of instantaneous sinuous structure in turbulent bouyant plumes. Waerme Stoffuebertragung 16, 237–242.

Biesheuvel, A., Wijngaarden, V., 1984. Two-phase flow equation for dilute dispersion of gas bubbles in liquid. J. Fluid Mech. 148, 301–318.

Cartellier, A., 1990. Optical probes for local void fraction measurements: characterization of performance. Rev. Sci. Instrum. 61, 871–874.

Cartellier, A., Achard, J.L., 1991. Local phase detection probes in fluid/fluid two-phase flow. Rev. Sci. Instrum. 62, 279–303.

Castillejos, A.H., Brimacombe, J., 1987. Measurement of physical characteristics of bubbles in gas–liquid plumes. Part ii: Local properties of turbulent air–water plumes in vertically injected jets. Metall. Trans. B 18, 659–671.

Climent, E., Magnaudet, J., 1999. Large-scale simulation of bubble-induced convection in a liquid layer. Am. Phys. Soc. 28, 4827–4830.

Davidson, J.K., Harrison, D., 1963. Fluidised Particles. Cambridge University Press, London.

Delnoj, E., Westerweel, J., Deen, N.G., Kuipers, J.A.M., Swaaij, W.P.M.V., 1999. Ensemble correlation PIV applied to bubble plumes rising in a bubble column. Chem. Eng. Sci. 54, 5159–5171.

Fannelop, T.K., Hirschberg, S., Kuffer, J., 1991. Surface current and recirculating cells generated by bubble curtains and jets. J. Fluid Mech. 229, 629–657.

George, W.K., Alpert, R.L., Tamanini, F., 1977. Turbulence measurements in an axisymmetric buoyant plume. Int. J. Heat Mass Transfer 20, 1145–1154.

Goossens, L., 1979. Reservoir Destratification with Bubble Plumes. Delft University Press.

Hassan, Y.A., Blanchat, T.K., Jr, Seeley, C.H., Jr, Canaan, R.E., 1992. Simultaneous velocity measurements of both components of a two-phase flow using particle image velocimetry. Int. J. Multiphase Flow 18 (3), 371–395.

Hassan, Y.A., Canaan, R.E., 1991. Full-field bubbly flow velocity measurements using a multiframe particle tracking technique. Exp. Fluids 12, 49–60.

Iguchi, M., Uemura, T., Yamamoto, F., Morita, Z., 1992. Multiphase flows in ironmaking and steel-making processes. Jpn J. Multiphase Flow 6, 54–64.

Keane, R.D., Adrian, R.J., 1990. Optimization of particle image velocimeters. Part i: Double pulsed systems. Meas. Sci. Technol. 1, 1202–1215.

Kobus, H.E., 1968. Analysis of the flow induced by air–bubble system. In: Proceedings of the 11th Conference on Coastal Engineering, vol. 2. London, England, pp. 1016–1031.

Lance, M., Bataille, J., 1991. Turbulence in the liquid phase of a uniform bubbly air–water flow. J. Fluid Mech. 222, 95–118.

Liu, W., Clark, N.N., 1995. Relationships between distributions of chord lengths and distributions of bubble sizes including their statistical parameters. Int. J. Multiphase Flow 21, 1073–1089.

Liu, W., Clark, N.N., Karamavruc, A.I., 1998. Relationships between bubble size distributions and chord-length distribution in heterogeneously bubbling systems. Chem. Eng. Sci. 53 (6), 1267–1276.

Milgram, J.H., 1983. Mean flow in round bubble plumes. J. Fluid Mech. 133, 345–376.

Mory, K., Sano, M., 1981. Process kinetic in injection metallurgy. Tetsu-to-HaganT 67, 672–695.

Mudde, R.F., Lee, D.J., Reese, J., Fan, L.S., 1997. Role of the coherent structures on Reynolds stresses in a 2-d bubble column. AIChE J. 43 (4), 913–926.

Parzen, E., 1962. On estimation of a probability density function and mode. Ann. Math. Stat. 33, 1065–1076.

Rensen, J., Roig, V., 2001. Experimental study of the unsteady structure of a confined bubble plume. Int. J. Multiphase Flow 27, 1431–1449.

Risso, F., Ellingsen, K., 2002. Velocity fluctuations in a homogeneous dilute dispersion of high-Reynolds-number rising bubbles. J. Fluid Mech. 453, 395–410.

Shah, Y.T., Kelkar, B.G., Gobole, S.P., Deckwer, W.D., 1982. Design parameter estimation for bubble column reactors. AIChE J. 28 (3), 353–379.

Sheng, Y.Y., Irons, G.A., 1992. Measurements of the internal structure of gas–liquid plumes. Metall. Trans. B 23B, 779–788.

Simiano, M., 2005. Experimental Investigation of Large-Scale Three Dimensional Bubble Plume Dynamics. Doctoral Thesis, ETH Diss. No. 16220, Zurich, Switzerland.

Simiano, M., Zboray, R., de Cachard, F., Lakehal, D., Yadigaroglu, G., 2004. Extensive measurements of the hydrodynamic characteristics of large scale bubble plumes. In: Proceedings of the 5th International Conference on Multiphase Flow. Yokohama, Japan.

Sjoen, K., 1983. Modelling of bubble plumes from subsea blowout. Doctoral Thesis, University of Trondheim UB/TIB Hannover D0-7069, Norway.

Tomiyama, A., 1998. Struggle with computational bubble dynamics. In: Proceedings of the 3rd International Conference on Multiphase Flow. Lyon, France.

van Wijngaarden, L., 1998. On pseudo turbulence. Theor. Comput. Fluid Dyn. 10, 449–458.

Walsche, C.D., de Cachard, F., 2000. Experimental investigation of condensation and mixing during venting of a steam/non-condensable gas mixture into a pressure suppression pool. In: Proceedings of the 98th International Conference on Nuclear Engineering (ICONE-8). Baltimore, Maryland, USA.

Wijngaarden, L.V., 1982. Hydrodynamic iterations in liquid gas flow. Appl. Sci. Res. 38, 331–339.

Wu, Q., Ishii, M., 1999. Sensitivity study on double-sensor conductivity probe for the measurement of interfacial area concentration in bubbly flow. Int. J. Multiphase Flow 25, 155–173.

Wu, Q., Welter, K., McCreary, D., Reyes, J.N., 1999. Design criteria and calibration of double-sensor probe for the measurement of bubble velocity. In: Proceedings of the 9th International Topical Meeting on Nuclear Reactor Thermal Hydraulics (NURETH-9). San Francisco, USA.

Zboray, R., Simiano, M., De Cachard, F., 2004. Local two-phase flow measurements with advanced data processing methods in bubbly plumes. In: Proceedings of the 3rd International Symposium on Two-Phase Flow Modelling and Experimentation. Pisa, Italy.